Anharmonic and Anomalous Trends in the High-Pressure Phase Diagram of Silicon

R. Paul, S. X. Hu, and V. V. Karasiev

Phys. Rev. Lett. **122**, 125701 — Published 25 March 2019

DOI: 10.1103/PhysRevLett.122.125701

Anharmonic and Anomalous Trends in the High-Pressure Phase Diagram of Silicon

R. Paul, S. X. Hu*, and V. V. Karasiev

Laboratory for Laser Energetics, University of Rochester, Rochester, New York 14623, USA

*e-mail: shu@lle.rochester.edu

ABSTRACT

A multifaceted *first-principles* approach utilizing density functional theory, evolutionary algorithms, and lattice dynamics was used to construct the phase diagram of silicon up to 4 TPa and 26000 K. These calculations predicted that (1) an anomalous sequence of face-centered cubic (fcc) to body-centered cubic (bcc) to simple cubic (sc) crystalline phase transitions occur at pressures of 2.87 TPa and 3.89 TPa, respectively, along the cold curve; (2) the orthorhombic phases of *Imma* and *Cmce-16* appear on the phase diagram only when the anharmonic contribution to the Gibbs free energy is taken into account; and (3) a substantial change in the slope of the principal Hugoniot is observed if the anharmonic free energy of the cubic diamond phase is considered.

Reliable pressure–temperature phase diagrams of matter, from *first-principles* electronic structure and phonon calculations [1–5] and experimental measurements [6–10], incorporate information on novel phases [11–14] that serve as the backbone of high-pressure materials science. As one of the most-abundant elements on Earth, silicon (Si) is of great interest to many fields encompassing industry [15], planetary science [16], geophysics [17], and high-energy-density (HED) physics [18,19]. For its importance to HED physics, the Hugoniot and the liquid phase of Si away from the melting curve has recently been explored thoroughly by *ab initio* calculations [20–24] and shock experiments up to pressures of 2.1 TPa [25–27]. However, the solid-state phase diagram of Si has been known from experiments only to a pressure range below 248 GPa and mostly along the 300 K isotherm [28–39].

For various solid crystalline structures of Si, experiments over the past decades have established the existence of the semiconductor cubic-diamond phase (Si-I: cd) up to around 12.5 GPa [28–35], followed by the metallic phases of β-tin (Si-II) in the 8.8-to-16 GPa [28–35], body-centered orthorhombic *Imma* (Si-XI) in the 13-to-16 GPa [36], simple hexagonal (Si-V: sh) in the 14-to-38 GPa [31–34], base-centered orthorhombic *Cmce* (Si-VI, previously called *Cmca*) in the 40-to-42 GPa [37], hexagonal close packed (Si-VII: hcp) in the 40-to-78 GPa [33,35,38], and face-centered cubic (Si-X: fcc) in the 78-to-248 GPa pressure regions [35,38]. At the much higher-compression pressures experimentally accessible today, it was still unknown in which phases Si crystallizes. Furthermore, the solid-state phase transitions experimentally verified so far (up to ~248 GPa) were limited to the room-temperature isotherm, along with cold compression curve *ab initio* calculations [40–42]; and the melting curve was largely unknown (experimental

observations only up to ~35 GPa [43–46]). A recent computational work [47] has examined a solid-state-only phase diagram up to 80 GPa without giving the melting line. The melting curve is essential not only for the completeness of a phase diagram but also to HED and other scientific applications. For example, knowing at what conditions shock-compressed Si melts is of great significance to inertial confinement fusion (ICF) target design using a Si ablator [18]. In addition, understanding the high-pressure chemistry involving Si-based coordination compounds inside super-Earth planets [48], where extremely high-pressure–temperature (*P–T*) conditions can be up to ~4700 GPa and ~18000 K, respectively, relies on an accurate and complete high *P–T* phase diagram with a known melting curve.

In this letter, we present the *first-principles* construction of a complete phase diagram of Si up to multi-TPa pressures, through lattice dynamics and density functional theory (DFT) [49] based electronic structure calculations. The calculated high *P–T* phase diagram of Si revealed new phases under multi-TPa conditions and also highlighted the importance of the anharmonic treatment during calculation of ionic-thermal Helmholtz free energy in order to predict accurate phase boundaries and the correct slope of the principal Hugoniot.

Our *first-principles* calculations were performed with the Vienna *ab initio* simulation package (VASP) [50–52] DFT code with a plane wave basis, which uses the Perdew–Burke–Ernzerhof (PBE) [53] generalized gradient approximation (GGA) [54] exchange-correlation functional and projector augmented wave (PAW) pseudopotentials [55] of 12 active electrons with an energy cutoff of 1100 eV. All calculations and fitting details including convergence tests can be found in the Supplementary Material [56].

Over the past decade, powerful evolutionary algorithm codes, such as XtalOpt [60], CALYPSO [61], and USPEX [62-64] were developed for predicting high-pressure crystalline structures. Here, we have employed USPEX for a pressure-based geometry and structure optimization with 16 different cases having N=1,2,3,..,16 atoms respectively in a conventional unit cell under periodic boundary conditions, with 3-5 searches being performed for each target pressure and N. The first generation of random structures had a population size of 10 to 40 structures, run over 20 to 40 subsequent generations until convergence. The structures having the lowest enthalpy were used as the seed for next-generation refinement. Each subsequent generation was created using 60% of the best structures of the previous generation by using a combination of heredity (65%), randomness (10%), rotational mutation (10%) and lattice mutation (15%). These structure searches resulted in eight candidate structures: cubic diamond (cd or Pearson symbol: *cF*8), body-centered tetragonal/beta-tin (bct/β-Sn or *tI*4), simple hexagonal (sh or *hP*1), hexagonal close-packed (hcp or *hP*2), double hexagonal close-packed (dhcp or *hP*4), face-centered cubic (fcc or *cF*4), body-centered cubic (bcc or *cI*2), and simple cubic (sc or *cP*1). These structures were considered for the cold compression curve (T = 0 K) calculations. It is noted that the dhcp, bcc, and sc phases have not yet been measured in experiments. In addition, we have also examined two other candidate structures: base-centered orthorhombic (*Cmce* or *oC*16) and body-centered orthorhombic (*Imma* or *oI*4). The *Cmce* structure was indicated in an x-ray diffraction experiment by Hanfland *et al.* [37] at pressures near 40 GPa, whereas the *Imma* phase was observed in the pressure range of 13 to 16 GPa in earlier experiments [36].

The lattice constants were varied, and axial ratios were optimized (for non-cubic structures) for each of these ten structures by performing single point calculations, such that these geometries created by the variations covered the entire pressure domain up to P = 4 TPa. For these modifications, we used 3×3 (diagonal) transformation matrices with strain rate ε being the controlling parameter. In such matrices, all the diagonal terms are $1+\varepsilon$ when first scaling the volume, while the second or third diagonal terms are replaced by $1/\sqrt{1+\varepsilon}$, when the axial (b/a or c/a) ratios are scaled subsequently by keeping the volume of the unit cell fixed. The internal parameters for three *Imma* (corresponding to pressures of 6.2 GPa, 10.7 GPa, and 17.9 GPa) and five *Cmce* (2.8 GPa, 10.9 GPa, 22.4 GPa, 35.1 GPa, and 47.9 GPa) geometries were optimized. For the rest, the internal parameters of the nearest lower pressure, for which optimization was performed, were used. Finally, the resulting discrete lattice Gibbs free energies (enthalpies) for each candidate structure at different pressures (zero temperature) were fitted with an augmented stabilized jellium model equation of state (ASJEOS) [65]:

$$G_{\text{cold}}\left(x, T = 0\ \text{K}\right) = \frac{a}{x^3} g(x) + \frac{b}{x^2} + \frac{c}{x} + d,$$

with $g(x) = 1 + \alpha(1-x)^4 - \beta(1-x)^5 + \gamma(1-x)^6$ and the volume ratio $x = v/v_0$. The ASJEOS fitting gives better results far away from equilibrium, than the more conventional third-order Birch–Murnaghan (BM) EOS [66] fitting.

Next, the finite-temperature thermodynamic variables were evaluated by performing integration over the phonon density of states (DOS). The force constants for

the *first-principles* phonon DOS calculations were obtained using the density functional perturbation theory (DFPT) [67] calculations in 128-atom supercells with the convergence criteria being the electronic energy error $<10^{-8}$ eV/atom and the ionic force error $<10^{-3}$ eV/Å. The results were thereafter used to solve the phonon eigenvalue problem [68,69], for eigenvalues of the Hessian of the phonon potential energy, and calculate the phonon spectra $Z(\omega)$. Within the quasi-harmonic approximation (QHA), the finite-temperature ionic contribution to the Helmholtz free energy $F_{\mathrm{i,QH}}$ was calculated using

$$F_{\mathrm{i,QH}} = F_{\mathrm{ZP}} + F_{\mathrm{i\text{-}th,QH}} = 3N\int_0^{\omega_{\max}}\left[\frac{\hbar\omega}{2} + k_{\mathrm{B}}T\ln\left(2\sinh\frac{\hbar\omega}{2k_{\mathrm{B}}T}\right)\right]Z(\omega)\,\mathrm{d}\omega$$

with $Z(\omega) = \frac{1}{3N}\sum_{\mathbf{k},j}\delta\left[\omega - \omega_j(\mathbf{k})\right]$ for a phonon wave vector $\mathbf{k}$ of band index j being normalized such that $\int_0^{\omega_{\max}} Z(\omega)\,\mathrm{d}\omega = 1$, where k_{B} is the Boltzmann constant, $\hbar$ is the reduced Planck constant, and N is the total number of ions. The first term corresponds to the quantum zero-point motion, whereas the latter corresponds to the thermal lattice-vibrational free energy. It was observed that the QHA breaks down for the *Cmce* and *Imma* phases, owing to negative phonon frequencies at zero Kelvin. In addition, finite-temperature dependence of their axial ratios renders the QH treatment inadequate in calculating the $F_{\mathrm{i\text{-}th}}(P,T)$. For these two phases, to calculate the harmonic free energy, a different reference system was used rather than the zero Kelvin system, akin to the method used for fcc–Fe [70]. Also, for the cubic diamond phase, significant deviations in

mapping of the $F_{\text{i-th,QH}}(P,T)$ manifests itself in an incorrect slope of the principal Hugoniot and will be explained later. These specific cases necessitated the introduction of an anharmonic correction term.

We resorted to the use of thermodynamic integration [71] for this correction, using the averaged internal energy U obtained from quantum molecular dynamics (QMD), and subtracting from it the ionic thermal kinetic energy, the U from the cold compression curve, and that from QHA. This was done with respect to a reference temperature T_{ref} such that $T_{\text{melting}} > T_{\text{ref}} > T_{\text{Debye}}$ and

$$\left\langle F_{i\text{-}th,AH}\left(T;T_{el}\to 0\right)\right\rangle_{\text{V}} = -T\int_{T_{\text{ref}}}^{T}\left.\frac{\left\langle U(T)\right\rangle_{QMD}-\left[U(T)\right]_{cold\ +\ i,QH}-\dfrac{3}{2}(N-1)k_BT}{T^2}\right|_{\text{V}}\mathrm{d}T$$

where T is the ionic temperature and T_{el} is the electronic one.

The finite-temperature electronic contribution to the Helmholtz free energy resulting from electronic thermal excitation ($F_{\text{e-th}}$) was calculated by performing single-point DFT calculations with Fermi–Dirac smearing corresponding to the ionic temperature. We found the anharmonic contribution $F_{\text{i-th,AH}}$ is generally of the same order of magnitude as the harmonic contribution especially for the cd, *Imma*, and *Cmce* phases [56]. The total Gibbs free energy $G(V,T) = G_{\text{cold}}(V,0) + F_{\text{i,QH}}(V,T) + F_{\text{i-th,AH}}(V,T) + F_{\text{e-th}}(V,T) + P_{\text{th}}V$, where the thermal pressure $P_{\text{th}} = P(V,T) - P(V,0)$, for an isotherm was fitted with

ASJEOS to obtain the analytic G along that isotherm. We could then identify the most stable phase in each (P,T) point by identifying the structure with the minimum G.

The results for the 300 K isotherm are shown by Fig. 1, in which the predicted *relative* Gibbs free energy for each structure is plotted as a function of pressure. Taking Fig. 1(a) as an example, the calculations show that the Imma phase is stable in the pressure range of 13.6 to 16 GPa, and the Cmce phase takes over for pressures between 33.2 GPa and 40.6 GPa. Fig. 1(b) indicates the fcc-to-bcc-to-sc transitions (the corresponding pressures are 2.87 TPa and 3.89 TPa respectively for $T = 0$ K).

To determine the melting curve, we have performed QMD simulations for canonical/constant-NVT ensemble in supercells with an initial solid structure in each phase under periodic boundary conditions. The temperature was controlled by a Nosé–Hoover thermostat [72]. The isochores for which melting point was evaluated had a range of density spanning from 2.33 g/cm^3 (for cd) to 21.27 g/cm^3 (for sc). This method for detecting the melting point was previously used to predict the melting curve of sodium [73,74]. A single special k point of (1/4, 1/4, 1/4) was used for sampling in the Brillouin zone (1BZ), as was introduced by A. Baldereschi [75]. The time step was varied from 0.26 to 0.63 fs, being an inverse function of the square root of temperature and the cube root of the density, with a total of 4000 to 6500 QMD steps for each density/temperature point. Converged results were reached with a large number (216 to 256) of atoms in a supercell.

Fig. 2 illustrates two examples of how we determine the melting point from QMD calculations for the solid–liquid transition for two isochores of $\rho = 2.57$ g/cm^3 in the cd phase and $\rho = 13.55$ g/cm^3 in the bcc phase. Figs. 2(a) and 2(b) indicate that at the

melting point, the pressure exhibits a discontinuity. The melting point (temperature, pressure) was considered to be the average of both sides of the discontinuity, e.g., (1475 K, 6.1 GPa) for cd and (23950 K, 3072.4 GPa) for bcc.

Figs. 2(a) and 2(b) imply that the pressure drop with increasing temperatures for the cd–solid to liquid transition correspond to an increase in density of Si upon melting, whereas a pressure jump for the bcc phase corresponds to a decrease in density. This opposing density change behaviors would imply a negative slope of the melting curve for the cd phase and a positive slope for the bcc phase, according to the Clausius–Clapeyron relation. This is proven to be true for the complete melting curve, to be shown in Fig. 3. Having obtained these discrete melting points for all phases up to 4 TPa, we fit them with the Kechin equation [76], a modified form of the Simon–Glatzel equation [77] with parameters a_i (i = 1,2,3) and (P_0,T_0), to all the (T_m,P_m) melting points

$$T_m(P_m) = T_0\left(1+\frac{P_m - P_0}{a_1}\right)^{a_2} e^{-a_3(P_m - P_0)}$$

in the cd and the other phases separately, to take into account the opposite slopes of the melting curve. The values of these constants for the negative slope branch of the melt curve is T_0 = 92.37 K, P_0 = 21.31 GPa, a_1 = 2.27 GPa, a_2 = 1.983, and a_3= 0.013; whereas the values for the remainder of the melt curve is T_0 = 10458.3 K, P_0 = 1114.48 GPa, a_1 = 783.56 GPa, a_2 = 4.565, and a_3 = 3.755. To further confirm the melting point derived from the pressure discontinuity, we also examined the ion–ion radial pair correlation function $g(\mathbf{r})$. Figs. 2(c) and 2(d) show a typical change in $g(\mathbf{r})$ at the solid-to-liquid transition

boundary [corresponding to the pressure discontinuity in Figs. 2(a) and 2(b)]. One can see that upon melting, the oscillation amplitude of $g(\mathbf{r})$ becomes monotonically decreasing, which is in contrast to the solid state.

Finally, the resulting high P–T phase diagram of Si up to 4 TPa and 26000 K is shown in Fig. 3. The available experimental measurements on the melt curve up to ~35 GPa are also compared. Overall, they are in good agreement with our melting temperature predictions within ±150 K. Given the imperfect crystal structures often encountered in experiments, the observed melting temperature being ~50 to 150 K lower than our predictions for a perfect crystal is reasonable since defects and anisotropy could initiate melting earlier. The previous experimental observation of different phases is also marked in Fig. 3 along the T = 300 K isotherm, which again agrees well with our calculated phases in the corresponding pressure ranges. The P-ρ EOS plot for 100 K, which demonstrates the density jumps upon phase transitions, also shows an approximately tenfold increase in density on compressing from ambient pressure to 4 TPa. The principal Hugoniot for a shock wave is determined by solving the Rankine–Hugoniot equation with our multiphase EOS data obtained in this work. The slightest inaccuracy in the initial internal energy E_0 could drastically affect the slope of the Hugoniot at low pressures, as can be seen in Fig. 3 on comparing the Hugoniot obtained by using the quasi-harmonic versus the anharmonic EOS data. The Hugoniot obtained inclusive of anharmonic calculations show agreement with recent experimental observations [46,78]. One interesting observation is that *Cmce* did not show up as a thermodynamically stable phase at T=0 K in our PBE-GGA calculations, although

previous LDA calculations [79] have shown *Cmce* to be stable for a narrow range of pressure along the cold curve.

A pressing question was to have a phenomenological explanation for the presence of the anomalous fcc-to-bcc-to-sc transition (with reduction in coordination number from 12-to-8-to-6) after a span of ~2.8 TPa, where fcc is stable. These high-pressure phases are dynamically stable with no negative phonon frequency found [56]. Upon detailed investigation of the electronic properties, we observed that a dip starts developing in the electronic DOS near the Fermi level, as can be seen in left side of Fig. 4(a-c). This dip becomes more pronounced with increasing pressures along the cold curve. The corresponding electron localization function (ELF) isosurface plot in the right side of Fig. 4(a-c) gives a more physical explanation of the trend in discussion. Electrons move from the hybridized orbital space to the interstitial space stabilizing the ionic structure at high pressures. Such a deviation from the expected free-electron-like behavior, causing structure change, has also been observed in the paired *Cmce* phase in dense lithium [80]. However, the dip never develops to a band gap, a phenomenon that leads to the formation of electrides, as is observed in elements like calcium [81].

In summary, we have constructed a high-pressure–temperature phase diagram of Si up to 4 TPa and 26,000 K, respectively, using *first-principles* electronic structure and phonon calculations. This yielded a new prediction on the existence of counterintuitive high-pressure fcc-to-bcc-to-sc transitions. After introducing anharmonic calculations, the *Imma* and *Cmce* phase were predicted on the phase diagram for the first time, matching earlier experimental observations.

We thank Dr. J. Ryan Rygg for useful discussions. This material is based upon work supported by the Department of Energy National Nuclear Security Administration under Award Number DE-NA0003856, the University of Rochester, and the New York State Energy Research and Development Authority.

References

1. T. Sjostrom, S. Crockett, and S. Rudin, Phys. Rev. B **94**, 144101 (2016).
2. D. Cebulla and R. Redmer, Phys. Rev. B **89**, 134107 (2014).
3. L. X. Benedict, K. P. Driver, S. Hamel, B. Militzer, T. Qi, A. A. Correa, A. Saul, and E. Schwegler, Phys. Rev. B **89**, 224109 (2014).
4. A. Lazicki, A. Dewaele, P. Loubeyre, and M. Mezouar, Phys. Rev. B **86**, 174118 (2012).
5. L. Caillabet, B. Canaud, G. Salin, S. Mazevet, and P. Loubeyre, Phys. Rev. Lett. **107**, 115004 (2011).
6. P. Loubeyre, F. Occelli, and R. LeToullec, Nature **416**, 613 (2002).
7. J. H. Eggert, D. G. Hicks, P. M. Celliers, D. K. Bradley, R. S. McWilliams, R. Jeanloz, J. E. Miller, T. R. Boehly, and G. W. Collins, Nat. Phys. **6**, 40 (2010).
8. S. Deemyad and I. F. Silvera, Phys. Rev. Lett. **100**, 155701 (2008).
9. C. S. Zha, H. Liu, J. S. Tse, and R. J. Hemley, Phys. Rev. Lett. **119**, 075302 (2017).
10. D. Errandonea, S. G. MacLeod, J. Ruiz-Fuertes, L. Burakovsky, M. I. McMahon, C. W. Wilson, J. Ibañez, D. Daisenberger, and C. Popescu, J. Phys.: Condens. Matter **30**, 295402 (2018).
11. T. Bi, D. P. Miller, A. Shamp, and E. Zurek, Angew. Chem. **129**, 10,326 (2017).
12. M. Hanfland, K. Syassen, N. E. Christensen, and D. L. Novikov, Nature **408**, 174 (2000).
13. C. J. Pickard and R. J. Needs, Nat. Mater. **9**, 624 (2010).

14. Y. Ma, M. Eremets, A. R. Oganov, Y. Xie, I. Trojan, S. Medvedev, A. O. Lyakhov, M. Valle, and V. Prakapenka, Nature **458**, 182 (2009).

15. G. J. Cheng, M. Cai, D. Pirzada, M. J. F. Guinel, and M. G. Norton, J. Manuf. Sci. Eng. **130**, 011008 (2008).

16. A. Benuzzi-Mounaix, S. Mazevet, R. Ravasio, T. Vinci, A. Denoeud, M. Koenig, N. Amadou, E. Brambrink, F. Festa, A. Levy *et al.*, Phys. Scr. **2014**, 014060 (2014).

17. Y. Zhang, T. Sekine, H. He, Y. Yu, F. Liu, and M. Zhang, Geophys. Res. Lett. **41**, 4554 (2014).

18. V. N. Goncharov, T. C. Sangster, R. Betti, T. R. Boehly, M. J. Bonino, T. J. B. Collins, R. S. Craxton, J. A. Delettrez, D. H. Edgell, R. Epstein *et al.*, Phys. Plasmas **21**, 056315 (2014).

19. S. X. Hu, G. Fiksel, V. N. Goncharov, S. Skupsky, D. D. Meyerhofer, and V. A. Smalyuk, Phys. Rev. Lett. **108**, 195003 (2012).

20. B. Militzer and K. P. Driver, Phys. Rev. Lett. **115**, 176403 (2015).

21. S. X. Hu, B. Militzer, L. A. Collins, K. P. Driver, and J. D. Kress, Phys. Rev. B **94**, 094109 (2016).

22. S. X. Hu, R. Gao, Y. Ding, L. A. Collins, and J. D. Kress, Phys. Rev. E **95**, 043210 (2017).

23. D. C. Swift, G. J. Ackland, A. Hauer, and G. A. Kyrala, Phys. Rev. B **64**, 214107 (2001).

24. O. Strickson and E. Artacho, Phys. Rev. B **93**, 094107 (2016).

25. T. Sano, A. Hirose, N. Ozaki, T. Kimura, K. Miyanishi, T. Endo, T. Jitsui, R. Kodama, Y. Sakawa, T. Mashimo *et al.*, Bull. Am. Phys. Soc. **54**, BAPS.2009.SHOCK.N1.71 (2009).

26. B. Henderson, D. Polsin, T. Boehly, M. Gregor, S. Hu, G. Collins, R. Rygg, D. Fratanduono, and P. Celliers, Bull. Am. Phys. Soc. **62**, BAPS.2017.SHOCK.T6.2 (2017).

27. P. Celliers, A. Ng, G. Xu, and A. Forsman, Phys. Rev. Lett. **68**, 2305 (1992).

28. J. C. Jamieson, Science **139**, 762 (1963).

29. P. Bundy, J. Chem. Phys. **41**, 3809 (1964).

30. J. Z. Hu, L. D. Merkle, C. S. Menoni, and I. L. Spain, Phys. Rev. B **34**, 4679 (1986).

31. H. Olijnyk, S. K. Sikka, and W. B. Holzapfel, Phys. Lett. A **103**, 137 (1984).

32. J. Z. Hu and I. L. Spain, Solid State Commun. **51**, 263 (1984).

33. A. Jayaraman, W. Klement, and G. C. Kennedy, Phys. Rev. **130**, 540 (1963).

34. J. F. Cannon, J. Phys. Chem. Ref. Data **3**, 781 (1974).

35. S. J. Duclos, Y. K. Vohra, and A. L. Ruoff, Phys. Rev. Lett. **58**, 775 (1987).

36. M. I. McMahon, R. J. Nelmes, N. G. Wright, and D. R. Allan, Phys. Rev. B **50**, 739 (1994).

37. M. Hanfland, U. Schwarz, K. Syassen, and K. Takemura, Phys. Rev. Lett. **82**, 1197 (1999).

38. S. J. Duclos, Y. K. Vohra, and A. L. Ruoff, Phys. Rev. B **41**, 12,021 (1990).

39. A. Mujica, A. Rubio, A. Munoz, and R. J. Needs, Rev. Mod. Phys. **75**, 863-912 (2003).

40. R. Ahuja, O. Eriksson, and B. Johansson, Phys. Rev. B **60**, 14,475 (1999).

41. R. J. Needs and A. Mujica, Phys. Rev. B **51**, 9652 (1995).

42. K. Gaál-Nagy and D. Strauch, Comput. Mater. Sci. **30**, 8 (2004).

43. V. V. Brazhkin, A. G. Lyapin, S. V. Popova, and R. N. Voloshin, Phys. Rev. B **51**, 7549 (1995).

44. J. Lees and B. H. J. Williamson, Nature **208**, 278 (1965).

45. A. Kubo, Y. Wang, C. E. Runge, T. Uchida, B. Kiefer, N. Nishiyama, and T. S. Duffy, J. Phys. Chem. Solids **69**, 2255 (2008).

46. S. J. Turneaure, S. M. Sharma, and Y. M. Gupta, Phys. Rev. Lett. **121**, 135701 (2018).

47. C. Li, C. Wang, J. Han, L. Yan, B. Deng, and X. Liu, J. Mater. Sci. **53**, 7475 (2018).

48. F. González-Cataldo, S. Davis, and G. Gutiérrez, Sci. Rep. **6**, 26537 (2016).

49. W. Kohn and L. J. Sham, Phys. Rev. **140**, A1133 (1965).

50. G. Kresse and J. Hafner, Phys. Rev. B **47**, 558 (1993); **49**, 14,251 (1994).

51. G. Kresse and J. Furthmüller, Comput. Mater. Sci. **6**, 15 (1996).

52. G. Kresse and J. Furthmüller, Phys. Rev. B **54**, 11,169 (1996).

53. J. P. Perdew, K. Burke, and M. Ernzerhof, Phys. Rev. Lett. **77**, 3865 (1996).

54. J. P. Perdew, J. A. Chevary, S. H. Vosko, K. A. Jackson, M. R. Pederson, D. J. Singh, and C. Fiolhais, Phys. Rev. B **46**, 6671 (1992); **48**, 4978(E) (1993).

55. P. E. Blöchl, Phys. Rev. B **50**, 17,953 (1994).

56. See the Supplemental Material at http://link.aps.org/supplemental/10.1103/PhysRevLett.xxx.xxxxxx for a more

detailed description of the computational method and convergence tests, which includes Refs. [57-59].

57. H. J. Monkhorst and J. D. Pack, Phys. Rev. B **13**, 5188 (1976).

58. P. Giannozzi, S. Baroni, N. Bonini, M. Calandra, R. Car, C. Cavazzoni, D. Ceresoli, G. L. Chiarotti, M. Cococcioni, I. Dabo, A. D. Corso, S. D. Gironcoli, S. Fabris, G. Fratesi, R. Gebauer, U. Gerstmann, C. Gougoussis, A. Kokalj, M. Lazzeri, L. Martin-Samos, N. Marzari, F. Mauri, R. Mazzarello, S. Paolini, A. Pasquarello, L. Paulatto, C. Sbraccia, S. Scandolo, G. Sclauzero, A. P. Seitsonen, A. Smogunov, P. Umari and R. M. Wentzcovitch, J. Phys.: Condens. Matter **21**, 395502 (2009).

59. P. Giannozzi, O. Andreussi, T. Brumme, O. Bunau, M. B. Nardelli, M. Calandra, R. Car, C. Cavazzoni, D. Ceresoli, M. Cococcioni, N. Colonna, I. Carnimeo, A. D. Corso, S. D. Gironcoli, P. Delugas, R. A. DiStasio Jr., A. Ferretti, A. Floris, G. Fratesi, G. Fugallo, R. Gebauer, U. Gerstmann, F. Giustino, T. Gorni, J. Jia, M. Kawamura, H. Y. Ko., A. Kokalj , E. Küçükbenli, M. Lazzeri, M. Marsili, N. Marzari, F. Mauri, N. L. Nguyen, H. V. Nguyen, A. Otero-de-la-Roza, L. Paulatto, S. Poncé, D. Rocca, R. Sabatini, B. Santra, M. Schlipf, A. P. Seitsonen, A. Smogunov, I. Timrov, T. Thonhauser, P. Umari, N. Vast, X. Wu and S. Baroni, J. Phys.: Condens. Matter **29**, 465901 (2017).

60. D. C. Lonie and E. Zurek, Comput. Phys. Commun. **182**, 372 (2011); **183**, 690 (2012).

61. Y. Wang, J. Lv, L. Zhu, and Y. Ma, Comput. Phys. Commun. **183**, 2063 (2012).

62. A. R. Oganov and C. W. Glass, J. Phys. Chem. **124**, 244704 (2006).

63. A. R. Oganov, A. O. Lyakhov, and M. Valle, Acc. Chem. Res. **44**, 227 (2011).

64. A. O. Lyakhov, A. R. Oganov, H. T. Stokes, and Q. Zhu, Comput. Phys. Commun. **184**, 1172 (2013).

65. A. B. Alchagirov, J. P. Perdew, J. C. Boettger, R. C. Albers, and C. Fiolhais, Phys. Rev. B **63**, 224115 (2001).

66. F. Birch, Phys. Rev. **71**, 809 (1947).

67. S. Baroni, S. de Gironcoli, A. Dal Corso, and P. Giannozzi, Rev. Mod. Phys. **73**, 515 (2001).

68. A. Togo, F. Oba, and I. Tanaka, Phys. Rev. B **78**, 134106 (2008).

69. A. Togo, L. Chaput, I. Tanaka, and G. Hug, Phys. Rev. B **81**, 174301 (2010).

70. L. Vocadlo, I. G. Wood, M. J. Gillan, J. Brodholt, D. P. Dobson, G. D. Price, and D. Alfè, Phys. Earth Planet. Inter. **170**, 52 (2008).

71. S. G. Moustafa, A. J. Schultz, E. Zurek, and D. A. Kofke, Phys. Rev. B **96**, 014117 (2017).

72. S. Nosé, Mol. Phys. **52**, 255 (1984).

73. E. R. Hernández and J. Íñiguez, Phys. Rev. Lett. **98**, 055501 (2007).

74. L. Koči, R. Ahuja, L. Vitos, and U. Pinsook, Phys. Rev. B **77**, 132101 (2008).

75. A. Baldereschi, Phys. Rev. B **7**, 5212 (1973).

76. V. V. Kechin, J. Phys.: Condens. Matter **7**, 531 (1995).

77. F. Simon and G. Glatzel, Z. Anorg. Allg. Chem. **178**, 309 (1929).

78. E. E. McBride, A. Krygier, A. Ehnes, E. Galtier, M. Harmand, Z. Konôpková, H. J. Lee, H.-P. Liermann, B. Nagler, A. Pelka, M. Rödel, A. Schropp, R. F. Smith, C. Spindloe, D. Swift, F. Tavella, S. Toleikis, T. Tschentscher, J. S. Wark, and A. Higginbotham, Nat. Phy. **15**, 89-94(2018).

79. N.E. Christensen, D.L. Novikov, and M. Methfessel, Solid State Commun. **110**, 615-619 (1999).

80. J. B. Neaton, and N. W. Ashcroft, Nature **400**, 141-144 (1999).

81. A. R. Oganov, Y. Ma, Y. Xu, I. Errea, A. Bergara, and A. O. Lyakhov, Proc. Natl. Acad. Sci. **107**, 7646 (2010).

Figure Captions

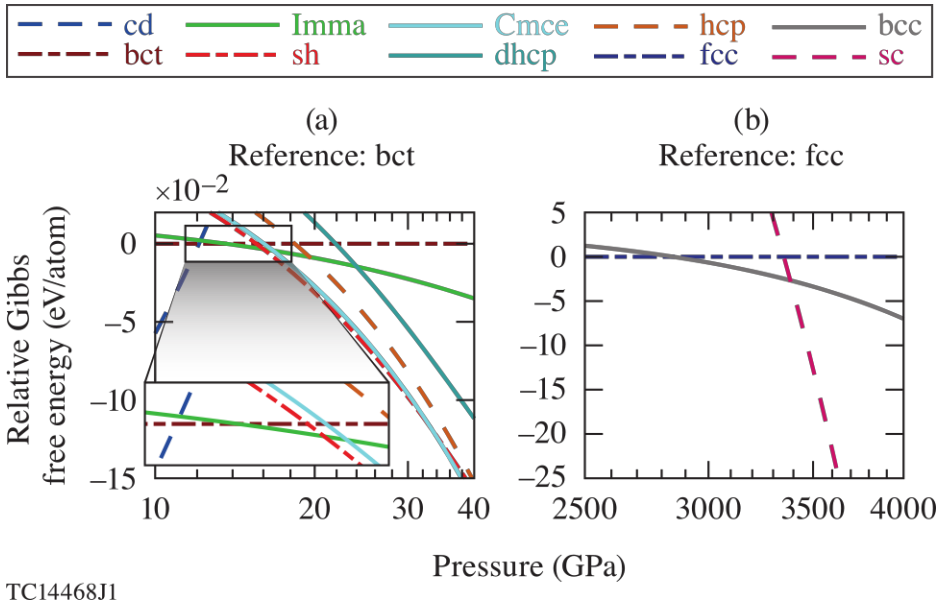

FIG. 1. The calculated Gibbs free energy for each phase at T = 300 K in (a) the low pressure and (b) the high pressure regions are plotted, which demonstrates six phase transitions: the cd–β-Sn transition at ~12 GPa, the β-Sn–Imma transition at ~14 GPa, the Imma–sh transition at 16 GPa, the sh–Cmce transition at ~33 GPa, the fcc–bcc transition at 2.8 TPa, and the bcc–sc transition at 3.4 GPa. The inset in (a) magnifies the 11-18 GPa region.

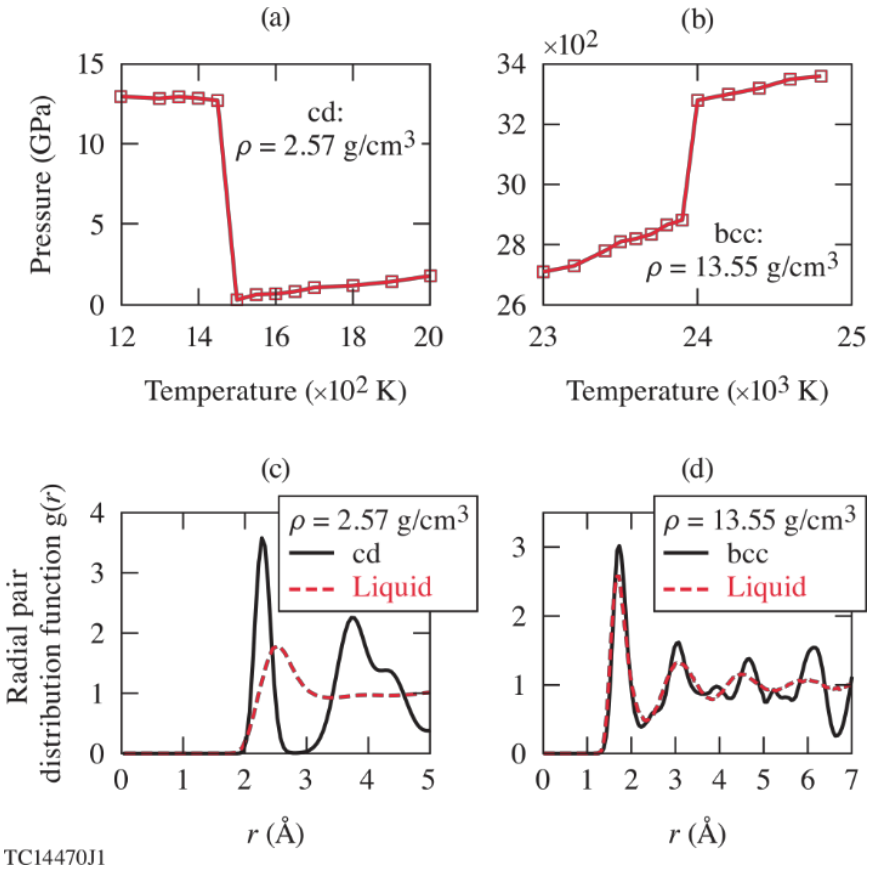

FIG. 2. The pressure discontinuity is used to determine the melting point for Si, e.g., in the (a) cd phase and (b) bcc phase. [(c), (d)] The change in $g(\mathbf{r})$ on the solid–liquid boundary.

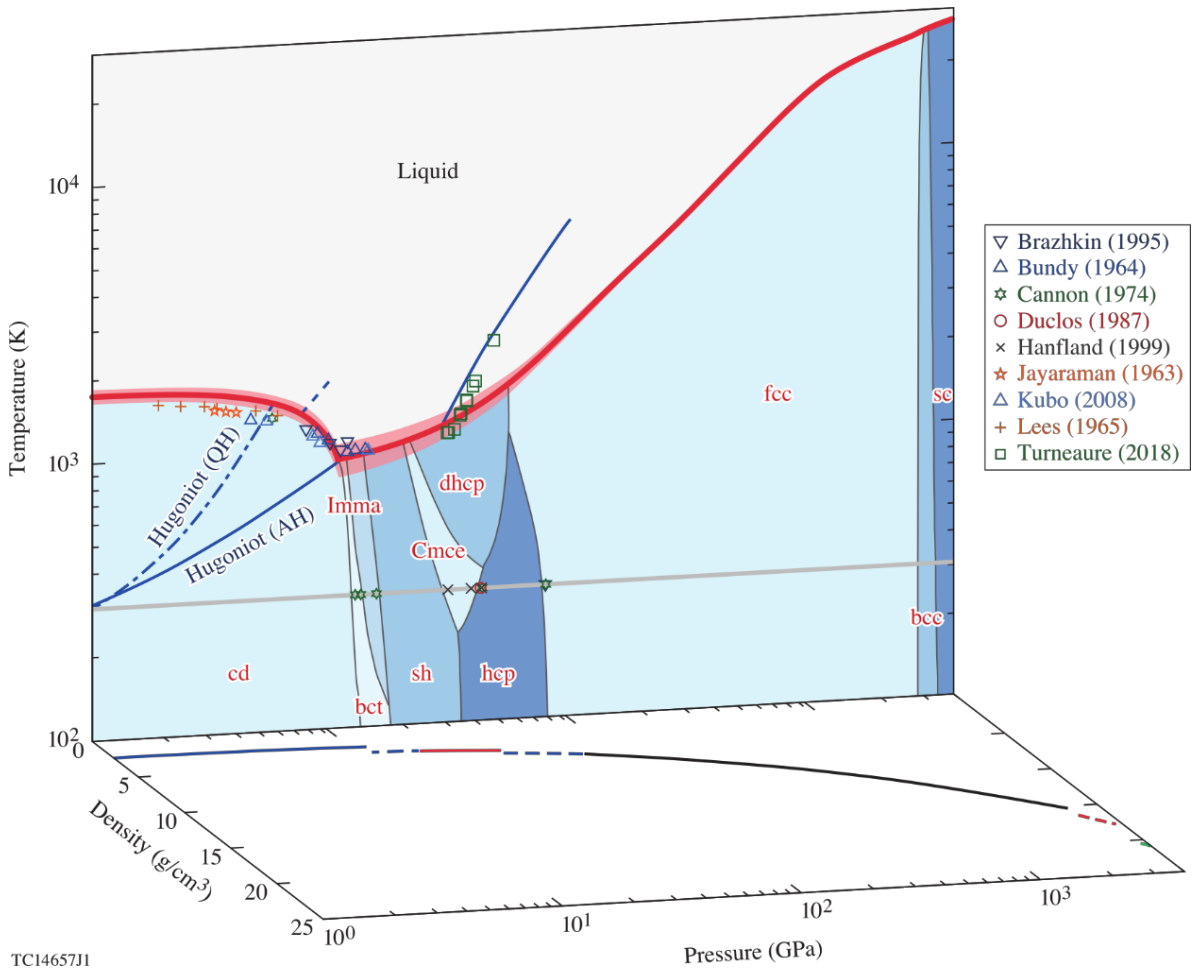

FIG. 3. The predicted high *P*–*T* phase diagram of Si with the gray horizontal line corresponding to the 300 K isotherm and the thick and dashed blue lines representing the principal Hugoniot using quasiharmonic (QH) and anharmonic (AH) analyses. The experimental results [29, 33–35, 37, 43–46] on melting and phase observations are marked by symbols. The shaded zone around the (red) melting curve denotes the uncertainty in our melting-curve calculations. Also, it should be noted that the Hugoniot (AH) meets the melting curve beyond the triple point.

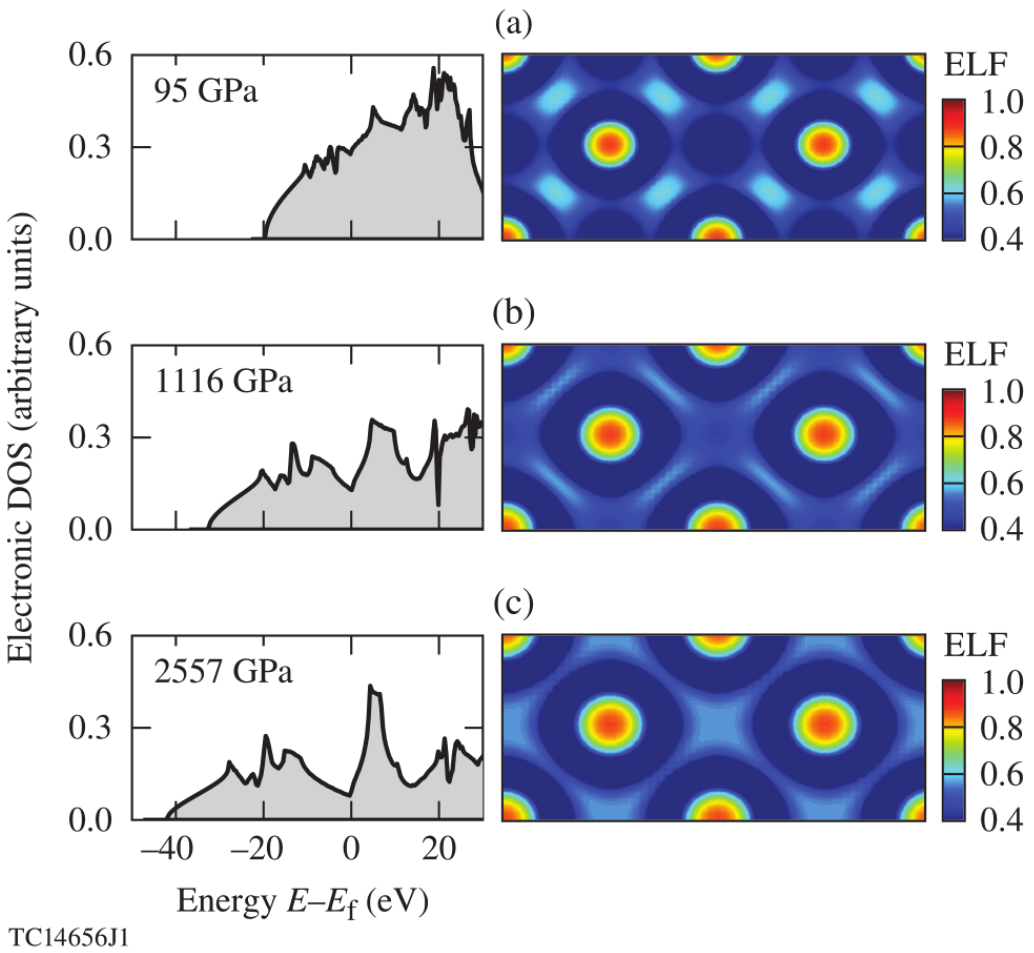

FIG. 4. The electronic density of state (DOS) and the electron localization function (ELF) for fcc–Si with increasing pressures. The Fermi energy (E_F) has been subtracted from the electronic energies.